CONDENSED MATTER PHYSICS

Variation of the giant intrinsic spin Hall conductivity of Pt with carrier lifetime

Lijun Zhu[1]*, Lujun Zhu[2], Manling Sui[3], Daniel C. Ralph[1,4], Robert A. Buhrman[1]

More than a decade after the first theoretical and experimental studies of the spin Hall conductivity (SHC) of Pt, both its dominant origin and amplitude remain in dispute. We report the experimental determination of the rapid variation of the intrinsic SHC of Pt with the carrier lifetime (τ) in the dirty-metal regime by incorporating finely dispersed MgO intersite impurities into the Pt, while maintaining its essential band structure. This conclusively validates the theoretical prediction that the SHC in Pt in the dirty-metal regime should be dominated by the intrinsic contribution, and should decrease rapidly with shortening τ. When interfacial spin backflow is taken into account, the intrinsic SHC of Pt in the clean limit is at least 1.6×10^6 ($\hbar/2e$) ohm^{-1} m^{-1}, more than 3.5 times greater than the available theoretical predictions. Our work also establishes a compelling spin Hall metal $Pt_{0.6}(MgO)_{0.4}$ with an internal giant spin Hall ratio of 0.73.

INTRODUCTION

Since the first theoretical and experimental efforts on its spin Hall conductivity (SHC) a decade ago (*1*–*4*), platinum (Pt), the archetypal spin Hall material, has been central in generating and detecting pure spin currents and key in establishing most of the recent spin-orbit coupling phenomena (*5*–*11*). However, the correct physical understanding of the SHC of Pt has remained unresolved, both qualitatively and quantitatively, despite the extensive attention that has been given to this intriguing condensed matter physics problem (*1*–*23*). The bulk spin Hall effect (SHE) of a heavy metal (HM) can have three possible contributions, i.e., the intrinsic contribution from the Berry curvature of the band structure and the extrinsic skew-scattering and side-jump contributions from spin-orbit interaction–related defect and impurity scattering (*24*). Theoretically, the intrinsic contribution should dominate the SHC of Pt in the dirty-metal and clean regimes where the carrier lifetime (τ) is short, whereas the extrinsic contributions can become important only in the ultraclean regime where τ is very long (see fig. S1) (*25*). A tight-binding model calculation by Tanaka *et al.* (*1*) has specified that a Pt sample is in the dirty-metal regime when its resistivity ($\rho_{xx} \propto \tau^{-1}$) is larger than ~30 microhm·cm. As a result, the intrinsic SHC of Pt, while being almost constant in the clean limit, is calculated to degrade rapidly with increasing ρ_{xx} or shortening τ in the dirty-metal regime [e.g., the calculated intrinsic SHC decreases from 2.6×10^5 to 1.6×10^5 then to 0.1×10^5 ($\hbar/2e$) ohm^{-1} m^{-1} as ρ_{xx} increases from 8 to 65 then to 200 microhm·cm (*1*)). Despite the consensus on the decrease of the SHC with τ in the dirty-metal regime, note that, quantitatively, the predicted clean-limit values of the intrinsic SHC (σ_{SH}) of Pt from the available theoretical calculations differ by more than a factor of 10 [i.e., σ_{SH} = (0.4 to 4.5) × 10^5 ($\hbar/2e$) ohm^{-1} m^{-1}] (*1*, *2*, *13*, *18*).

Experimentally, the characteristic variation of the intrinsic SHC with τ in the dirty-metal regime has never been quantified because it is a challenge to tune τ over a large range without varying the band structure and the Berry curvature. For example, in the composition-dependent studies on Pt-based binary alloys (e.g., $Pd_{1-x}Pt_x$ or $Au_{1-x}Pt_x$) (*14*, *16*, *18*), the source of the SHC is the new alloy phase rather than Pt, as indicated by the greater SHC in the more resistive $Au_{1-x}Pt_x$ and $Pd_{1-x}Pt_x$ phases than that in Pt. Also, there is a substantial change in the lattice constant (tensile strain) of the material upon alloying (*14*, *16*), which first-principles calculations (*26*) have indicated to significantly alter the SHC of Pt. In previous composition- or thickness-dependent studies (*14*, *16*, *18*, *23*), the increase of the damping-like spin-orbit torque (SOT) efficiency per unit bias current density (ξ^j_{DL}) with increasing ρ_{xx} was not a definitive indication of an intrinsic SHC because the side-jump contribution to ξ^j_{DL} can also increase with ρ_{xx}. Since $\xi^j_{DL} = T_{int}\sigma_{SH}\rho_{xx}$, with T_{int} being the spin transparency of the HM/ferromagnet (FM) interface, the experimental situation can also have an additonal complication when the HM layer is thinner than four times of its spin diffusion length (λ_s). This is because raising ρ_{xx} can increase T_{int} (see Eq. 3) by shortening λ_s of the HM ($\lambda_s \propto 1/\rho_{xx}$ in the Elliott-Yafet spin relaxation mechanism) (*27*, *28*) and thus can affect spin backflow (SBF) when the HM thickness is not $>>4\lambda_s$ (*29*, *30*). Last, in a recent temperature-dependent nonlocal spin valve study of Pt with varying ρ_{xx} (*15*), the amplitudes and the variations of σ_{SH} are both comparable with the reported measurement uncertainty in the dirty-metal regime, preventing any examination of the variation of the intrisic σ_{SH} of Pt with ρ_{xx} and thus τ.

There is also a strong disagreement between experiments on the amplitude of σ_{SH} in Pt in the clean limit. Direct SOT measurements (*31*) reveal a lower bound value of $\approx 1.5 \times 10^6$ ($\hbar/2e$) ohm^{-1} m^{-1} for the intrinsic σ_{SH} of Pt with $\rho_{xx} \approx$ 30 to 50 microhm·cm when the less than unitary T_{int} due to SBF (*29*, *30*) and spin memory loss (SML) at the Pt/FM interfaces (*31*–*33*) is taken into account. In contrast, the nonlocal spin valve study (*15*) where all the interfaces were assumed to be fully spin-transparent reported a small constant σ_{SH} of 0.3 × 10^6 ($\hbar/2e$) ohm^{-1} m^{-1} for both dirty and clean limits (ρ_{xx} = 6 to 80 microhm·cm). Generally, since the bare spin-mixing conductance at an HM/FM interface ($G^{\uparrow\downarrow}_{HM/FM}$) is only comparable to the spin conductance of the HM (G_{HM}) rather being infinite, the drift-diffusion model (*29*, *30*) predicts that an SBF will substantially reduce T_{int}, e.g., by more than 50% for Pt/FM interfaces. This has been unambiguously confirmed by the discovery of the spin Hall magnetoresistance in Pt/FM systems (*34*). Any SML due to substantial interfacial spin-orbit scattering (ISOC) at the interface (*31*) will further decrease T_{int}. Clarifying the underlying physics of the giant SHC of Pt is both of fundamental interest and of technological urgency (e.g., for maximizing ξ^j_{DL} for low-power devices). Arguably, Pt and certain Pt-rich alloys

[1]Cornell University, Ithaca, NY 14850, USA. [2]College of Physics and Information Technology, Shaanxi Normal University, Xi'an 710062, China. [3]Institute of Microstructure and Property of Advanced Materials, Beijing University of Technology, Beijing 100124, China. [4]Kavli Institute at Cornell, Ithaca, NY 14853, USA.
*Corresponding author. Email: zhulijun0@gmail.com

(*14*, *16*) are the most attractive class of spin Hall metals for energy-efficient spin-torque applications because their combination of the highest SHC of any known class of metals with comparatively low ρ_{xx} provides a high ξ^j_{DL} and minimal current shunting into an adjacent FM at the same time.

In this work, we report a substantial (×3) tuning of carrier mean lifetime τ in Pt films by varying the concentration of MgO intersite impurities (Fig. 1A) while maintaining the long-range face-centered-cubic (fcc) order of the Pt. From this, we observe a rapid degradation (×5) of the intrinsic SHC of Pt with decreasing τ in the dirty-metal regime, providing the first experimental validation of the tight-binding model prediction of the characteristic variation of the intrinsic SHC of Pt with carrier lifetime (*1*). We are also able to exclude both extrinsic and interfacial mechanisms as important contributions to the SHC of Pt over the investigated resistivity range (30 microhm·cm ≤ ρ_{xx} ≤ 240 microhm·cm). These results conclusively establish that the dominant source of the giant SHC in Pt in the dirty-metal regime is the bulk intrinsic SHE arising from the Berry curvature of its band structure. This

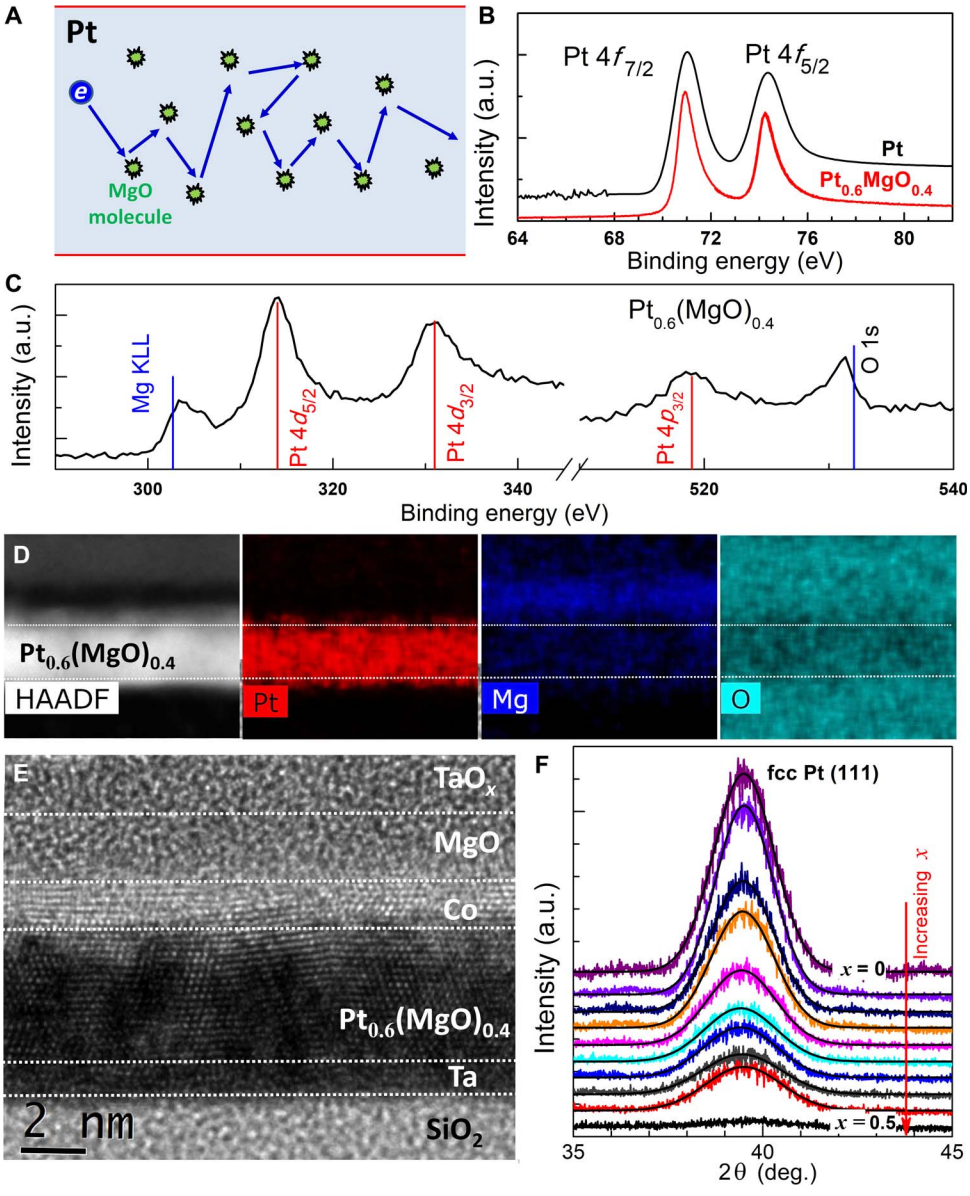

Fig. 1. Sample structure. (**A**) Schematic of enhanced impurity scattering in Pt by finely dispersed MgO molecules. (**B**) XPS spectrum for Pt 4*f* peaks in a $Pt_{0.6}(MgO)_{0.4}$ layer (black line) and a pure Pt layer (red line), indicating non-oxidation of Pt in both cases. a.u., arbitrary units. (**C**) XPS spectrum for Pt 4*d* and 4*p* peaks, Mg KLL peak, and O 1s, indicating that Pt atoms are not oxidized while Mg and O atoms coexist as MgO molecules in the $Pt_{1-x}(MgO)_x$ layer peak. The solid lines represent the peak positions expected for nonbonding instances. Different from the Pt peaks, the Mg KLL and O 1s peaks show clear shifts of ±0.8 eV in binding energy, suggesting that Pt is not oxidized while Mg is oxidized. (**D**) Cross-sectional high-angle annular dark field scanning transmission electron microscopy (HAADF-STEM) image and energy-dispersive x-ray spectroscopy mapping of Pt, Mg, and O, showing no indication of Pt or MgO clusters. The two dotted lines represent the upper and lower interfaces of the $Pt_{0.6}(MgO)_{0.4}$ layer. (**E**) Cross-sectional high-resolution transmission electron microscopy image (bright field) of a magnetic stack of Ta 1/ $Pt_{0.6}(MgO)_{0.4}$ 4/Co 1.4/MgO 2/TaO_x 1.5. (**F**) XRD θ-2θ patterns for $Pt_{1-x}(MgO)_x$/Co bilayers with different *x*, indicating the robustness of the long-range fcc order of Pt (peak position) in the presence of increasing MgO impurities (peak weakening and broadening).

also establishes the limit to which θ_{SH} can be increased by shortening the carrier lifetime of Pt. Moreover, the giant experimental SHC values for Pt (e.g., $\geq 1.6 \times 10^6$ ($\hbar/2e$) ohm^{-1} m^{-1} in the clean limit) indicate that the existing first-principles and tight-binding theories (*1*, *2*, *12*, *13*, *18*) are underestimating the true intrinsic SHC in Pt by more than a factor of 3.5. Last, we achieve a 100% enhancement in ξ^j_{DL} by increasing ρ_{xx} via the incorporation of MgO impurities into Pt. This establishes a new ternary spin Hall material $Pt_{0.6}(MgO)_{0.4}$ that is very compelling for low-power SOT applications because of its combination of a giant θ_{SH}, a comparably low ρ_{xx}, a large Dzyaloshinskii-Moriya interaction (DMI), and easy growth on silicon substrates by sputtering.

RESULTS AND DISCUSSION

Sample structure

Multilayer stacks of Ta 1.0/$Pt_{1-x}(MgO)_x$ 4.0/Co 0.68 to 1.4/MgO 2.0/Ta 1.5 (numbers are thickness in nanometers) with MgO volume percentage x = 0, 0.05, 0.1, 0.15, 0.2, 0.25, 0.3. 0.35, 0.4, and 0.5, respectively, were sputter-deposited on Si/SiO_2 substrates. The $Pt_{1-x}(MgO)_x$ layer was co-sputtered from a Pt target and a MgO target. The Co magnetization (M_s) for these samples was measured by a vibrating sample magnetometer to be ~1220 ± 85 electromagnetic unit/cm^3, indicating the absence of an important magnetic proximity effect (*22*) in these as-grown samples. We find from x-ray photoemission spectroscopy (XPS) studies (Fig. 1B) that the Pt $4f_{7/2}$ and $4f_{5/2}$ peaks are located at 71.1 and 74.4 eV, respectively, in both a $Pt_{0.6}(MgO)_{0.4}$ and a pure Pt layer. In contrast, the binding energies of $4f_{7/2}$ and $4f_{5/2}$ peaks for Pt oxides are reported to be shifted to ~72.3 and ~75.8 eV for Pt^{2+} and to 74.0 and 77.5 eV for Pt^{4+}, respectively (*35*, *36*). Meanwhile, we find that the XPS peaks for Mg KLL and O 1s are shifted by ≈±0.8 eV, respectively (Fig. 1C). This indicates that, in the $Pt_{1-x}(MgO)_x$ layers, the Pt atoms are not oxidized while the Mg atoms are oxidized, and Mg and O coexist as MgO molecules, consistent with the fact that Pt has a much stronger electronegativity than Mg. Figure 1D shows cross-sectional energy-dispersive x-ray spectroscopy (EDS) Pt, Mg, and O mapping of the composite material $Pt_{0.6}(MgO)_{0.4}$ under the high-angle annular dark field scanning transmission electron microscopy (HAADF-STEM) mode (a relatively low-resolution mode). This indicates, within the resolution, that the MgO molecules are finely dispersed within the Pt. High-resolution cross-sectional transmission electron microscopy (TEM) studies of the Pt(MgO) composites [see Fig. 1E for imaging of a $Pt_{0.6}(MgO)_{0.4}$ sample] show that the co-sputtered $Pt_{1-x}(MgO)_x$ layer has a homogeneous polycrystalline texture where the grains are ~4 nm in vertical extent and that there is no indication of the presence of Pt or MgO clusters of observable size. The high-resolution transmission electron microscopy (TEM) result in Fig. 1E indicates that the long-range fcc order of Pt is essentially maintained despite the high-concentration MgO impurities (x = 0.4 in Fig. 1E). This is further reaffirmed by the x-ray diffraction (XRD) θ-2θ patterns of $Pt_{1-x}(MgO)_x$ 4/Co 1.4 bilayers in Fig. 1F. The $Pt_{1-x}(MgO)_x$ layer shows a broad fcc (111) peak due to the polycrystalline texture and the small thickness. However, unlike the case for Pt alloyed with another fcc metal (*14*, *16*), the fcc (111) peak for all different values of x does not shift with x but is located at the Bragg angle of Pt for all different x, indicating that the diffraction is from the periodic Pt lattice and that the MgO molecules are primarily dispersed in the Pt as intersite impurities rather than being substituted into the Pt lattice. However, the Pt (111) peaks do show a marked broadening and weakening with increasing x (see fig. S3) due to the increasing presence of MgO impurities and the reducing Pt atomic volume. We also note here that, in this XRD measurement configuration where the grain size along the film normal is the film thickness (~4 nm; see Fig. 1E), the broadening of the Pt (111) peaks does not indicate a variation of the Pt grain size. It is somewhat unexpected that the lattice periodicity of Pt is so resilient against a large degree of MgO incorporation. A more detailed high-resolution analysis in the future can be useful for better understanding this material, but it is beyond the scope of the present work.

Resistivity and carrier lifetime

We determined the average resistivity ρ_{xx} for the $Pt_{1-x}(MgO)_x$ layers for each x by measuring the conductance enhancement of the corresponding stacks with respect to a reference stack with no $Pt_{1-x}(MgO)_x$ layer. Note that the average resistivity ρ_{xx} best describes the effective scattering (by impurities, interfaces, and phonons) that a charge carrier experiences when flowing in the $Pt_{1-x}(MgO)_x$ layer (see Fig. 1A and fig. S2) and directly determines the charge current density (j_e) via $j_e = E/\rho_{xx}$ for a given applied electric field E. As summarized in Fig. 2A, ρ_{xx} for the $Pt_{1-x}(MgO)_x$ is enhanced by a factor of ~8, i.e., increases gradually from 33 microhm·cm at x = 0 (pure Pt) to 74 microhm·cm for x = 0.4, and then jumps up to 240 microhm·cm for x = 0.5. These high values of ρ_{xx} (>30 microhm·cm) place the $Pt_{1-x}(MgO)_x$ films with $0 \leq x \leq 0.5$ in the dirty-metal regime as calculated by Tanaka *et al.* (*1*) and as indicated by our experimental results discussed below. The increase in ρ_{xx} with x is due, in part, to the increase in carrier scattering rate ($1/\tau$) and, in part, to the decrease in charge carrier density $n = n_{Pt}(1-x)$. To separate these two contributions, we use the Drude model approximation for the resistivity

$$\rho_{xx} = 1/\sigma_{xx} = m^*/ne^2\tau \quad (1)$$

where σ_{xx} is the electrical conductivity and m^* is the effective mass of the charge carriers. In this approximation, the carrier lifetime in $Pt_{1-x}(MgO)_x$ is

$$\tau = \sigma_{xx}m^*/ne^2 \approx \tau_{Pt}\sigma_{xx}/\sigma_{xx,Pt}(1-x) \quad (2)$$

where $\sigma_{xx,Pt}$ and $\tau_{Pt} = \sigma_{xx,Pt}m^*/ne^2$ are the electrical conductivity and the carrier lifetime of the 4-nm pure Pt film (x = 0). As shown in Fig. 2B, with increasing impurity concentration x, τ for $Pt_{1-x}(MgO)_x$ decreases monotonically from τ_{Pt} for x = 0, moderately to $0.74\tau_{Pt}$ for x = 0.4, and then more abruptly to $0.27\tau_{Pt}$ for x = 0.5. We speculate that the modest increase in the carrier scattering rate with the MgO incorporation for x up to 0.4 is due to the very small scattering cross section of MgO molecules, while the substantial increase in scattering rate when x is increased from 0.4 to 0.5 may be due to an increase of very small MgO aggregates with a higher scattering cross section at that higher MgO content.

Physical origin of the giant SHC in Pt

In the following, we determine that the dominant source of the Pt SHC is the intrinsic SHE. We first calculated the apparent SHC $\sigma^*_{SH} \equiv T_{int}\sigma_{SH} = (\hbar/2e)\xi^E_{DL}$ as a function of x from our experimental results in Fig. 2C. Here, $\xi^E_{DL} = \mu_0 M_s t H_{DL}/E$ is the damping-like SOT per applied electric field (*23*), μ_0 is the permeability of vacuum, t is the ferromagnetic layer thickness, and H_{DL} is the damping-like SOT effective field for E = 66.7 kV/m as determined from harmonic

response measurements (see figs. S4 and S5 and section S1) (*14*, *16*, *31*). Note that the thickness (d) and the carrier density (thus σ_{xx}) of the HM are not involved in the calculation of σ_{SH}^{*} and ξ_{DL}^{E}. In good accord with the changes in τ caused by the MgO addition, σ_{SH}^{*} decreases only moderately from 4.9×10^5 $(\hbar/2e)$ ohm^{-1} m^{-1} at $x = 0$ to 4.1×10^5 $(\hbar/2e)$ ohm^{-1} m^{-1} at $x = 0.4$ and then sharply drops to 1.3×10^5 $(\hbar/2e)$ ohm^{-1} m^{-1} at $x = 0.5$.

To obtain the internal values of $\sigma_{SH} = \sigma_{SH}^{*}/T_{int}$, T_{int} of the $Pt_{1-x}(MgO)_x$/Co interfaces has to be calculated for each x. With the drift-diffusion analysis (*29*, *30*), the interfacial spin transparency set by the SBF is given by

$$T_{int} = [1 - \mathrm{sech}(d/\lambda_s)]/\left[1 + G_{HM}\tanh(d/\lambda_s)/2G_{HM/FM}^{\uparrow\downarrow}\right] \quad (3)$$

where $G_{HM} = \sigma_{xx}/\lambda_s$ is spin conductance of the HM. Because $G_{HM/FM}^{\uparrow\downarrow}$ typically scales with the Sharvin conductance G_{Sh} of the HM and both G_{Sh} (*37*) and G_{HM} are proportional to n and independent of τ, we have $G_{Pt-MgO} = (1 - x)G_{Pt}$ and $G_{Pt-MgO/Co}^{\uparrow\downarrow} = (1 - x)G_{Pt/Co}^{\uparrow\downarrow}$. Assuming a dominant Elliott-Yafet spin relaxation mechanism ($\lambda_s \propto \sigma_{xx}$) (*29*, *30*) and using the experimental value $G_{Pt} \approx 1.3 \times 10^{15}$ ohm^{-1} m^{-2} (*23*) and the theoretical value $G_{Pt/Co}^{\uparrow\downarrow} \approx 0.59 \times 10^{15}$ ohm^{-1} m^{-2} (*30*), we estimated that λ_s of $Pt_{1-x}(MgO)_x$ decreases monotonically from 2.35 nm for $x = 0$, to 1.73 nm for $x = 0.4$ and 0.64 nm for $x = 0.5$ (fig. S5B) and that T_{int} of the $Pt_{1-x}(MgO)_x$/Co interface increases monotonically from 0.32 for $x = 0$ to 0.39 for $x = 0.4$ and 0.47 for $x = 0.5$ (fig. S5C).

Now, we can examine the effect of τ on the SHC. In Fig. 2D, we compare our experimental results of σ_{SH}^{*} and $\sigma_{SH} = \sigma_{SH}^{*}/T_{int}$ for different x to the theoretical predictions of intrinsic SHC as a function of $\sigma_{xx}/(1 - x)$. Here, we use $\sigma_{xx}/(1 - x) \propto \tau$ as an approximate linear indicator of τ. Functionally, the scaling of σ_{SH} and σ_{SH}^{*} with $\sigma_{xx}(x)/(1 - x)$ and thus with τ is quite consistent with the tight-binding model prediction (*1*). The 4-nm-thick pure Pt sample with a relatively low $\sigma_{xx,Pt} = 3 \times 10^6$ ohm^{-1} m^{-1} due to the strong scattering at its interfaces is just on the predicted crossover from the clean limit to the dirty-metal regime with respect to its intrinsic SHC behaviors. As τ is gradually decreased by increasing x, the intrinsic SHC decreases monotonically, in accord with the theoretical prediction (*1*, *25*) (see also fig. S1) for the variation of σ_{SH} with electrical conductivity (τ) in the dirty-metal regime. The amplitude of the measured SHC is quite different from the predicted values, but if we rescale the magnitude of the tight-binding model result by a constant factor of 6 (Fig. 2D), then we find good agreement between the experiment and the prediction. Therefore, the tight-binding model captures the functional form, but not the magnitude, of the experimental behavior. More specifically, our experiment and the tight-binding model prediction (*1*) establish that the giant SHC of Pt is dominated by intrinsic Berry curvature contribution in the clean and dirty-metal regimes and that the intrinsic SHC varies strongly with the carrier lifetime τ in the dirty-metal regime. The good qualitative consistency of the experiment and theory also indicates that the topology of the Fermi surface of the fcc Pt is rather robust to the intersite impurities but is, as predicted, quite sensitive to τ in this high-resistivity regime. This establishes a practical limit to which θ_{SH} of pure Pt can be enhanced (i.e., $\theta_{SH} \approx 0.65$; see fig. S6) solely by reducing τ even if the structure order can be maintained while reducing τ. We do note that there is a minor difference between the experimental data of σ_{SH} and the rescaled tight-binding model prediction (×6) in the dirty-metal regime, which we tentatively attribute to a small SML at the $Pt_{1-x}(MgO)_x$/Co interfaces. As established previously (*31*), SML can result from ISOC of the HM/FM interface and

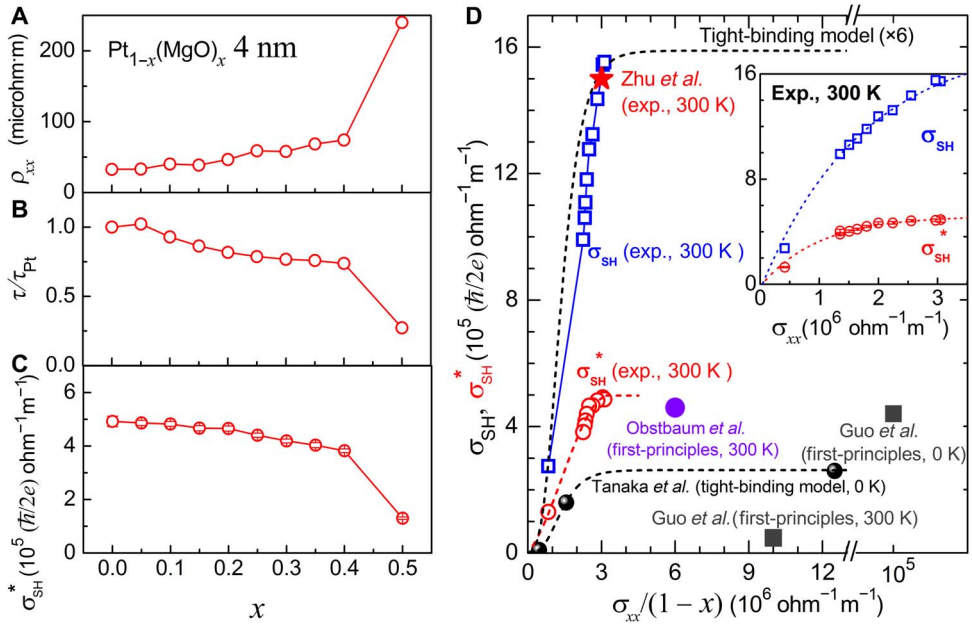

Fig. 2. Variation of the SHC with carrier lifetime. The experimental values of (**A**) the average resistivity, (**B**) carrier lifetime, (**C**) the apparent SHC (σ_{SH}^{*}) for $Pt_{1-x}(MgO)_x$ 4/Co 1.4 bilayers plotted as a function of MgO concentration (x) of the $Pt_{1-x}(MgO)_x$ layers. (**D**) Experimental and theoretical values for the (apparent) SHC of Pt plotted as a function of $\sigma_{xx}/(1 - x)$, with $\sigma_{xx}/(1 - x)$ being an approximate linear indicator of carrier lifetime. Inset: Nonlinear dependence of the experimental values of σ_{SH}^{*} and σ_{SH} on σ_{xx}. In (D), the black dots, gray squares, and violet dot represent σ_{SH} of Pt predicted by the tight-binding model and first-principles calculations in the studies of Tanaka *et al.* (*1*), Guo *et al.* (*2*), and Obstbaum *et al.* (*18*), respectively. The red star represents the experimental value of σ_{SH} of Pt determined in (*31*). The dashed lines in (D) are solely to guide the eyes.

increases linearly with the interfacial perpendicular magnetic anisotropy energy density of the HM/FM interface ($K_s^{HM/FM}$). Using the same method as in (*31*), we determined that $K_s^{Pt-MgO/Co}$ for these unannealed in-plane $Pt_{1-x}(MgO)_x$/Co samples gradually decreases from ~0.66 erg/cm^2 for $x = 0$ to be negligible for $x = 0.5$ (see fig. S7). These overall small amplitudes of ISOC [compared to the sample with a substantial SML in (*31*)] are well consistent with the high amplitude of σ_{SH} of the low-MgO concentration samples being close to that of Pt/Co samples after SML correction (the red star in the Fig. 2D). The MgO dopants may also interrupt the perfection of the long-range fcc order of Pt and thus may contribute to the difference between the measured and rescaled theoretical values of σ_{SH}. This, however, should be a minor effect compared to the dominant role of the carrier lifetime in determining the variation of σ_{SH}.

We now exclude the extrinsic skew scattering and side jump as important mechanisms in contributing to the SHC of Pt. As shown in the inset of Fig. 2D, the obvious nonlinear relations between σ_{xx} and σ_{SH} (with an SBF correction) and between σ_{xx} and σ_{SH}^* (without an SBF correction) for different x obviously disagree with a dominant skew-scattering mechanism ($\sigma_{SH} \propto \sigma_{xx}$). This is consistent with the theoretical expectation that the skew scattering should not be important in the dirty-metal regime. With regard to the possibility of a side-jump contribution to σ_{SH} of Pt and $Pt_{1-x}(MgO)_x$, we can draw from the conclusions of previous studies of side-jump contribution to the anomalous Hall conductivity (AHC) (*38*). Such research indicates that the side-jump contribution to σ_{SH} should scale inversely with the square of the residual resistivity ratio (RRR = ρ_{xx}/ρ_{xx0}) of the metal, where ρ_{xx0} is the residual, low-temperature resistivity due to elastic defect scattering. As shown in fig. S8, the RRR for our pure Pt sample ($x = 0$) is approximately 1.4, while RRR ≈ 1.1 for $x = 0.4$. Therefore, if the side jump was dominant, then we should expect a 60% increase in σ_{SH} as x increases from 0 to 1.1. In light of the decrease in σ_{SH} between $x = 0$ and $x = 0.4$, we can rule out side jump as an important contributor to the SHC of Pt and $Pt_{1-x}(MgO)_x$ in the dirty-metal limit. The AHC of some FMs (e.g., $L1_0$-ordered MnGa, MnAl, or FePt) (*39*–*41*) may have a distinguishable extrinsic SHC even in the "dirty-metal" regime, but in that case, the intrinsic AHC is very small—at least two orders of magnitude smaller than the intrinsic SHC of Pt. Therefore, we conclude that the intrinsic contribution is the dominant physical origin of the observed SHC in Pt.

An interfacial origin of the SHC can also be safely ruled out as a significant factor in the Pt/Co and $Pt_{1-x}(MgO)_x$/Co systems. The clear qualitative correlation between the evolution of σ_{SH}^* over the entire range ($0 < x \leq 0.5$) and the changes in carrier lifetime of the Pt films confirms that the SOTs that we observe in this system are the result of a bulk effect [i.e., due to the SHC from the long-range fcc order of Pt in the $Pt_{1-x}(MgO)_x$ layer] rather than an interfacial effect. This conclusion of a predominant bulk origin of the SOTs in our doped Pt system is consistent with the previously reported rapid decrease of the SOT strength (σ_{SH}^*) when the Pt or Pt alloy thickness becomes less than $4\lambda_s$ (*14*, *16*, *23*). Here, we take note of a recent report of a strong SOT from a Pt oxide/NiFe interface (*35*). In that case, there was no current flow in the insulating Pt oxide ($\rho_{xx} = 2.2 \times 10^7$ microhm·cm), which is in sharp contrast to our case where the current is flowing in the conductive $Pt_{1-x}(MgO)_x$ layer. Thus, the Pt oxide/NiFe does not have any connection to our $Pt_{1-x}(MgO)_x$/Co study.

After having established the intrinsic nature of the Pt SHC, we return to the quantitative comparison of the measured SHC results to the available theoretical predictions. Even before we make any corrections for the effect of the thickness of the sample compared to its λ_s and less than perfect T_{int}, the experimental values that we obtain for σ_{SH}^* are equal to or larger than the available theoretical predictions for Pt from first-principles or tight-binding calculations (see the comparison in Fig. 2D). If we only consider the ideal situation of SBF being important, with no additional SML (*31*–*33*), then the experiments determine the actual intrinsic SHC of 1.1×10^6 to 1.6×10^6 ($\hbar/2e$) ohm^{-1} m^{-1} for $\sigma_{xx} > 2.2 \times 10^5$ ohm^{-1} m^{-1}(or $\rho_{xx} \leq 74$ microhm·cm) (see Fig. 2D). In the clean limit (e.g., $\rho_{xx} \leq 32$ microhm·cm), the actual intrinsic SHC of Pt is then at least ~1.6×10^6 ($\hbar/2e$) ohm^{-1} m^{-1}. This is significantly larger than any of the existing theoretical predictions, that is, 0.4×10^5 to 4.5×10^5 ($\hbar/2e$) ohm^{-1} m^{-1} (*1*, *2*, *12*, *13*, *18*), indicating that the available theoretical calculations are underestimating the true intrinsic SHC of Pt by more than a factor of 3.5, most likely more because there can be SML at Pt/Co interfaces (*31*–*33*). We infer that there is still important underlying physics related to the generation of spin currents by intrinsic effects in Pt that is yet to be fully understood and that could benefit from the additional theoretical investigation.

Practical impact for low-power SOT devices

θ_{SH} and ξ_{DL}^j are the most direct parameters that characterize the useful strength of the phenomenon. Figure 3A shows the results for $\theta_{SH} = (2e/\hbar)\sigma_{SH}\rho_{xx}$ for the $Pt_{1-x}(MgO)_x$ layers and $\xi_{DL}^j = T_{int}\theta_{SH} = \xi_{DL}^E\rho_{xx}$ for the $Pt_{1-x}(MgO)_x$ 4/Co 1.4 bilayers, where the HM thickness of 4 nm is chosen from the viewpoint of the optimized current efficiency of a SOT switching of magnetic tunneling junctions (*42*). In consistence with the bulk intrinsic SHE, θ_{SH} increases monotonically from 0.51 for pure Pt to 0.73 for $x = 0.4$ and then slightly drops back to 0.66 for $x = 0.5$ because of the strong decrease in σ_{SH} as the result of the sharp decrease in carrier lifetime. We note that $\theta_{SH} = 0.73$ is still a low bound value for $Pt_{0.6}(MgO)_{0.4}$ as there is still SML. The internal value of θ_{SH} for $Pt_{0.6}(MgO)_{0.4}$ would be ≈0.95 if the difference between the experimental and rescaled tight-binding model values of σ_{SH} in Fig. 2D is attributed solely to the SML. Note that $\theta_{SH} \approx 0.95$ should be the upper bound for the case where Pt is diluted by an insulator (e.g., MgO here) that does not alter the band structure. This upper limit ($\theta_{SH} \approx 0.95$) is higher than that for pure Pt ($\theta_{SH} \approx 0.65$) because, for the same σ_{SH} and τ, the enhancement of ρ_{xx} for $Pt_{0.6}(MgO)_{0.4}$ is more significant than that in pure Pt because of the additional dilution effect of the carrier density in $Pt_{0.6}(MgO)_{0.4}$. Benefiting from the increase of both θ_{SH} and T_{int} (fig. S5) with x, ξ_{DL}^j increases from 0.16 at $x = 0$ (33 microhm·cm) to 0.28 at $x = 0.4$ (74 microhm·cm). At $x = 0.5$, despite the result that ρ_{xx} increases sharply to 240 microhm·cm, ξ_{DL}^j only slightly increases to 0.31. The giant ξ_{DL}^j of ≈0.3 that we obtained with the 4-nm $Pt_{0.6}(MgO)_{0.4}$ ($\rho_{xx} = 74$ microhm·cm) is comparable to the high value reported for fcc-$Au_{0.25}Pt_{0.75}$ ($\rho_{xx} \approx 83$ microhm·cm) (*16*) and β-W ($\rho_{xx} \approx 300$ microhm·cm) (*43*) and three times higher than that of β-Ta ($\rho_{xx} \approx 190$ microhm·cm) (*44*). The SHE in those HMs has been demonstrated to enable sub-nanosecond deterministic magnetic memories (*8*, *42*), gigahertz and terahertz oscillators (*9*, *10*), and fast skyrmion/chiral domain wall devices (*11*, *44*). However, for low-power device applications, new HMs that simultaneously combine a giant ξ_{DL}^j with a low ρ_{xx} and a good compatibility for device integration are still urgently required (*14*, *16*). In that regard, we first point out that $Pt_{0.6}(MgO)_{0.4}$ ($\xi_{DL}^j = 0.28$ and $\rho_{xx} = 74$ microhm·cm) is as efficient as $Pd_{0.25}Pt_{0.75}$ (*14*) and $Au_{0.25}Pt_{0.75}$ (*16*) and progressively more so than Pt, β-W (*43*), β-Ta (*44*), and the topological insulator Bi_xSe_{1-x} ($\xi_{DL}^j = 3.5$ to 18.6) (*46*, *47*) for

SOT applications with metallic magnets, e.g., in-plane magnetized FeCoB/MgO magnetoresistive random access memories (MRAMs; see the quantitative comparison in Table 1), after taking into account the current shunting into the ferromagnetic layer (see fig. S9 and section S2 for details on the power calculations). The $Pt_{0.6}(MgO)_{0.4}$ is also better than Pt, β-W, and β-Ta in current efficiency. The relatively small ρ_{xx} of the $Pt_{0.6}(MgO)_{0.4}$ is also highly desirable for applications that require high energy/current efficiencies but small write impedance, e.g., the prospective implementation of SOT devices in cryogenic computing systems (*48*). In that case, the very resistive spin Hall materials of β-W (*43*), β-Ta (*44*), and Bi_xSe_{1-x} (*46*, *47*) are all problematic.

As an independent check of the validity of the strong damping-like SOT generated by the $Pt_{1-x}(MgO)_x$, we show in Fig. 3, B and C the sharp deterministic switching of a perpendicularly magnetized Co layer through domain wall depinning driven by the strong damping-like SOT generated by the SHE in a 4-nm $Pt_{0.7}(MgO)_{0.3}$ layer [we use $Pt_{0.7}(MgO)_{0.3}$ rather than $Pt_{0.6}(MgO)_{0.4}$ to provide a stronger perpendicular magnetic anisotropy and a larger coercivity]. The Co layer has a thickness of 0.68 nm, a coercivity (H_c) of ~80 Oe (Fig. 3D), and an effective perpendicular anisotropy field (H_k) of ~2.0 T as determined by fitting the dependence of $V_{1\omega}$ on the in-plane bias field H_x following the parabolic relation $V_{1\omega} = \pm V_{AH}(1 - H_x^2/2H_k^2)$ (see Fig. 3E). The switching current of ~2.7 mA (Fig. 3, B and C)

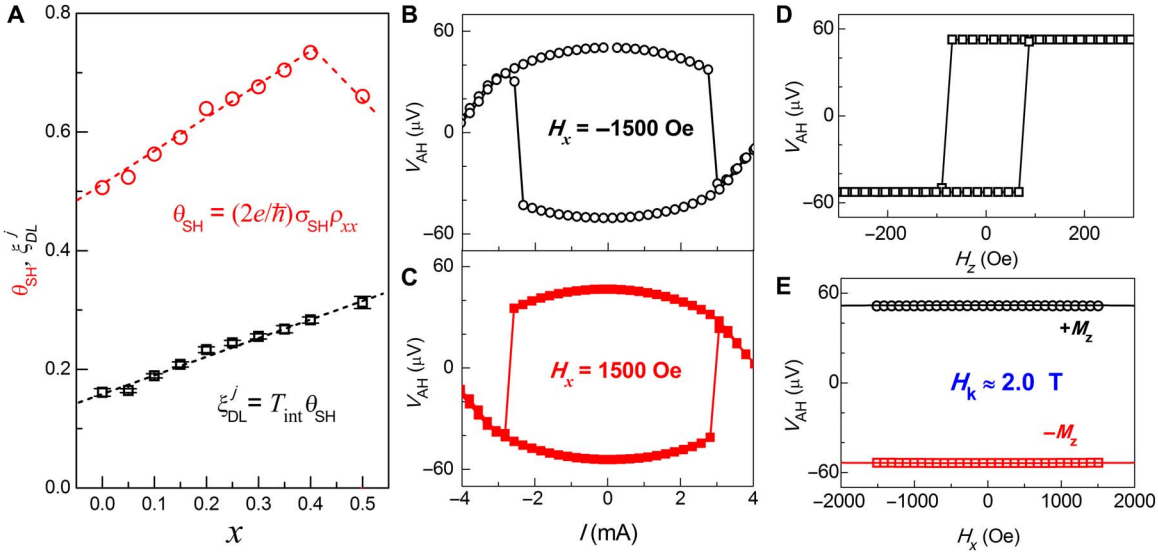

Fig. 3. Spin Hall ratio, damping-like SOT efficiency, and current-induced switching of perpendicular magnetization. (**A**) The MgO concentration dependence of θ_{SH} and ξ^j_{DL} for the $Pt_{1-x}(MgO)_x$ 4/Co 1.4 bilayers. (**B**) V_{AH} versus I (H_x = −1500 Oe), (**C**) V_{AH} versus I (H_x = 1500 Oe), (**D**) V_{AH} versus H_z, and (**E**) V_{AH} versus H_x for the $Pt_{0.7}(MgO)_{0.3}$ 4/Co 0.68 bilayers. The Hall bar dimension is 5 μm by 60 μm. The applied electric field is E = 1.67 kV/m for (B) to (E).

Table 1. Comparison of ξ^j_{DL}, θ, ρ_{xx}, $\sigma^*_{SH}(x)$ and calculated power and current consumption of SOT-MRAM devices for various strong spin current generators. Here, we use a spin Hall channel (600 nm by 300 nm by 4 nm), an FeCoB free layer (190 nm by 30 nm by 1.8 nm; resistivity ≈ 130 microhm·cm), and the parallel resistor model for the illustrative calculation (see the Supplementary Materials for details on the power and current calculations). Power and current are normalized to that of the $Pt_{0.6}(MgO)_{0.4}$-based device. n.a., not applicable.

	ξ^j_{DL}	θ_{SH}	ρ_{xx} (microhm·cm)	σ^*_{SH} [10^5 ($\hbar$/2e) ohm^{-1} m^{-1}]	Power	Current	Reference
$Pt_{0.6}(MgO)_{0.4}$	0.28	>0.73	74	3.8	1.0	1.0	This work
$Pd_{0.25}Pt_{0.75}$	0.26	>0.6	58	4.5	0.9	1.0	(*14*)
$Au_{0.25}Pt_{0.75}$	0.3	>0.6	83	3.6	1.0	0.95	(*16*)
Pt	0.16	0.51	33	4.9	1.2	1.6	This work
Bi_2Se_3	3.5	n.a.	1755	2.0	2.6	0.3	(*46*)
$Pt_{0.5}(MgO)_{0.5}$	0.31	0.66	240	1.3	4.5	1.2	This work
β-W	0.3	n.a.	300	1.0	7.1	1.3	(*43*)
β-Ta	0.12	n.a.	190	0.63	21	2.8	(*44*)
Bi_xSe_{1-x}	18.6	n.a.	13000	1.4	25	0.4	(*47*)

corresponds to a critical switching current density of $j_e = 1.15 \times 10^7$ A/cm^2 in the $Pt_{0.7}(MgO)_{0.3}$ layer. To obtain reliable switching in this configuration, it was necessary to apply an in-plane magnetic field of >1000 Oe along the current direction to overcome the domain wall chirality imposed by the DMI at the HM/Co interface (*49*).

Here, we also note that the requirement of a large in-plane bias field (>1000 Oe) for switching perpendicular magnetization indicates a strong DMI at the $Pt_{1-x}(MgO)_x$ /FM interface, which, together with the high ξ^j_{DL}, makes $Pt_{1-x}(MgO)_x$ particularly attractive for energy-efficient skyrmion and chiral domain wall devices driven by SHE-governed domain wall depinning (*11*, *49*). However, such a bias field is not required for the anti-damping SOT switching of collinear or "*y*-type" in-plane magnetized magnetic memories (*50*), which have been demonstrated to be unexpectedly efficient and fast [e.g., critical switching current (density) of ~110 μA (~5×10^6 A/cm^2) and ~200 ps for W-based FeCoB-MgO MRAM devices (*42*)].

CONCLUSION

We have presented the first experimental observation of the rapid variation of the intrinsic SHC of Pt with the carrier lifetime in the dirty-metal regime, a characteristic of the intrinsic SHC as theoretically predicted more than a decade ago. Via tuning the scattering from the finely dispersed MgO intersite impurities, the carrier lifetime τ and intrinsic SHC were varied by factors of 3 and 5, respectively, while the basic fcc order of Pt was maintained. We have also excluded any important skew-scattering, side-jump, or interfacial contributions to the SHE in this system. These results unambiguously determine the dominant intrinsic nature of the giant SHE in the archetypal material of Pt and establish the limit to which the spin Hall efficiency of Pt can be enhanced by shortening τ (i.e., $\theta_{SH} \approx 0.65$ for pure Pt). Moreover, the internal intrinsic SHC in the clean limit is experimentally found to be $>1.6 \times 10^6$ $(\hbar/2e)$ ohm^{-1} m^{-1}, a value that is considerably underestimated by the existing first-principles and tight-binding theories. Our effort in shortening τ via MgO incorporation into Pt also enables a 100% enhancement of ξ^j_{DL} for the $Pt_{0.6}(MgO)_{0.4}$/Co bilayers compared to the Pt/Co bilayer. This establishes a new spin Hall material $Pt_{0.6}(MgO)_{0.4}$ that is very compelling for low-power SOT applications in magnetic memories, oscillators, and skyrmion/chiral domain wall devices because of its combination of a giant spin Hall ratio ($\theta_{SH} = 0.73$ with a upper bound of ≈0.95 if the SML is diminished) with a relatively low resistivity (~74 microhm·cm), a strong DMI, and a good compatibility with the fabrication requirements for integrated circuit technologies.

MATERIALS AND METHODS

All the samples were sputter-deposited at room temperature on Si/SiO_2 substrates with an argon pressure of 2 mtorr and a base pressure of below 1×10^{-8} torr. The volume percentage (*x*) of MgO in the $Pt_{1-x}(MgO)_x$ layers was determined using the calibrated growth rates of Pt and MgO. The 1-nm Ta underlayer was introduced to improve the adhesion and the uniformity of the stack. The 1.5-nm Ta capping layer was fully oxidized upon exposure to the atmosphere. The magnetization of Co layers and the chemical bond information in the $Pt_{1-x}(MgO)_x$ layers were measured by a vibrating sample magnetometer and XPS, respectively. The sample structure was also characterized by combining cross-sectional high-resolution TEM imaging, HAADF-STEM imaging, and EDS mapping in a spherical aberration–corrected (Cs-corrected) 300-kV FEI Titan G2 microscope equipped with a Super-X detector. A focused ion beam (FEI Helios Nanolab 600i) was used during the preparation of the STEM samples. The stacks were patterned into Hall bars with a dimension of 5 μm by 60 μm by ultraviolet photolithography and argon ion milling for harmonic response measurements and direct current switching experiments. In the magnetization switching experiment, the dc current was sourced by a Yokogawa 7651, and the differential Hall resistance was detected by the lock-in amplifier ($E = 1.67$ kV/m).

SUPPLEMENTARY MATERIALS

Supplementary material for this article is available at http://advances.sciencemag.org/cgi/content/full/5/7/eaav8025/DC1

Fig. S1. Evolution of SHC with carrier lifetime.
Fig. S2. Three carrier scattering schemes.
Fig. S3. Composition dependence of the intensity and the full width at half maximum of the XRD patterns.
Fig. S4. Determination of SOT effective fields.
Fig. S5. MgO concentration dependence of spin-torque fields, spin diffusion length, and interfacial spin transparency.
Fig. S6. Enhancement of the spin Hall ratio in Pt by shortening carrier lifetime.
Fig. S7. MgO concentration dependence of interfacial magnetic anisotropy energy density.
Fig. S8. Temperature dependence of resistivity for 4-nm-thick Pt and $Pt_{0.6}(MgO)_{0.4}$ films.
Fig. S9. Schematics of a SOT-MRAM device.
Section S1. In-plane harmonic response measurements
Section S2. Calculation of power consumption of SOT-MRAM devices

REFERENCES AND NOTES

1. T. Tanaka, H. Kontani, M. Naito, T. Naito, D. S. Hirashima, K. Yamada, J. Inoue, Intrinsic spin Hall effect and orbital Hall effect in *4d* and *5d* transition metals. *Phys. Rev. B* **77**, 165117 (2008).
2. G. Y. Guo, S. Murakami, T.-W. Chen, N. Nagaosa, Intrinsic spin Hall effect in platinum: First-principles calculations. *Phys. Rev. Lett.* **100**, 096401 (2008).
3. E. Saitoh, M. Ueda, H. Miyajima, G. Tatara, Conversion of spin current into charge current at room temperature: Inverse spin-Hall effect. *Appl. Phys. Lett.* **88**, 182509 (2006).
4. T. Kimura, Y. Otani, T. Sato, S. Takahashi, S. Maekawa, Room-temperature reversible spin Hall effect. *Phys. Rev. Lett.* **98**, 156601 (2007).
5. H. Nakayama, M. Althammer, Y.-T. Chen, K. Uchida, Y. Kajiwara, D. Kikuchi, T. Ohtani, S. Geprägs, M. Opel, S. Takahashi, R. Gross, G. E. W. Bauer, S. T. B. Goennenwein, E. Saitoh, Spin Hall magnetoresistance induced by a nonequilibrium proximity effect. *Phys. Rev. Lett.* **110**, 206601 (2013).
6. K. Uchida, S. Takahashi, K. Harii, J. Ieda, W. Koshibae, K. Ando, S. Maekawa, E. Saitoh, Observation of the spin Seebeck effect. *Nature* **455**, 778–781 (2008).
7. S. Y. Huang, X. Fan, D. Qu, Y. P. Chen, W. G. Wang, J. Wu, T. Y. Chen, J. Q. Xiao, C. L. Chien, Transport magnetic proximity effects in platinum. *Phys. Rev. Lett.* **109**, 107204 (2012).
8. S. V. Aradhya, G. E. Rowlands, J. Oh, D. C. Ralph, R. A. Buhrman, Nanosecond-timescale low energy switching of in-plane magnetic tunnel junctions through dynamic Oersted-field-assisted spin Hall effect. *Nano Lett.* **16**, 5987–5992 (2016).
9. V. E. Demidov, S. Urazhdin, H. Ulrichs, V. Tiberkevich, A. Slavin, D. Baither, G. Schmitz, S. O. Demokritov, Magnetic nano-oscillator driven by pure spin current. *Nat. Mater.* **11**, 1028–1031 (2012).
10. Y. Wu, M. Elyasi, X. Qiu, M. Chen, Y. Liu, L. Ke, H. Yang, High-performance THz emitters based on ferromagnetic/ nonmagnetic heterostructures. *Adv. Mater.* **29**, 1603031 (2017).
11. P. P. J. Haazen, E. Murè, J. H. Franken, R. Lavrijsen, H. J. M. Swagten, B. Koopmans, Domain wall depinning governed by the spin Hall effect. *Nat. Mater.* **12**, 299–303 (2013).
12. G. Y. Guo, Q. Niu, N. Nagaosa, Anomalous Nernst and Hall effects in magnetized platinum and palladium. *Phys. Rev. B* **89**, 214406 (2014).
13. D. Go, D. Jo, C. Kim, H.-W. Lee, Intrinsic spin and orbital Hall effects from orbital texture. *Phys. Rev. Lett.* **121**, 086602 (2018).
14. L. Zhu, K. Sobotkiewich, X. Ma, X. Li, D. C. Ralph, R. A. Buhrman, Strong damping-like spin-orbit torque and tunable Dzyaloshinskii–Moriya interaction generated by low-resistivity $Pd_{1-x}Pt_x$ alloys. *Adv. Funct. Mater.* **29**, 1805822 (2019).
15. E. Sagasta, Y. Omori, M. Isasa, M. Gradhand, L. E. Hueso, Y. Niimi, Y. Otani, F. Casanova, Tuning the spin Hall effect of Pt from the moderately dirty to the superclean regime. *Phys. Rev. B* **94**, 060412(R) (2016).
16. L. Zhu, D. C. Ralph, R. A. Buhrman, Highly efficient spin current generation by the spin Hall effect in $Au_{1-x}Pt_x$. *Phys. Rev. Applied* **10**, 031001 (2018).

17. M.-H. Nguyen, M. Zhao, D. C. Ralph, R. A. Buhrman, Enhanced spin Hall torque efficiency in $Pt_{100-x}Al_x$ and $Pt_{100-x}Hf_x$ alloys arising from the intrinsic spin Hall effect. *Appl. Phys. Lett.* **108**, 242407 (2016).
18. M. Obstbaum, M. Decker, A. K. Greitner, M. Haertinger, T. N. G. Meier, M. Kronseder, K. Chadova, S. Wimmer, D. Ködderitzsch, H. Ebert, C. H. Back, Tuning Spin hall angles by alloying. *Phys. Rev. Lett.* **117**, 167204 (2016).
19. A. J. Berger, E. R. J. Edwards, H. T. Nembach, O. Karis, M. Weiler, T. J. Silva, Determination of the spin Hall effect and the spin diffusion length of Pt from self-consistent fitting of damping enhancement and inverse spin-orbit torque measurements. *Phys. Rev. B* **98**, 024402 (2018).
20. G. V. Karnad, C. Gorini, K. Lee, T. Schulz, R. Lo Conte, A. W. J. Wells, D.-S. Han, K. Shahbazi, J.-S. Kim, T. A. Moore, H. J. M. Swagten, U. Eckern, R. Raimondi, M. Kläui, Evidence for phonon skew scattering in the spin Hall effect of platinum. *Phys. Rev. B* **97**, 100405(R) (2018).
21. J. W. Lee, Y.-W. Oh, S.-Y. Park, A. I. Figueroa, G. van der Laan, G. Go, K.-J. Lee, B.-G. Park, Enhanced spin-orbit torque by engineering Pt resistivity in $Pt/Co/AlO_x$ structures. *Phys. Rev. B* **96**, 064405 (2017).
22. L. J. Zhu, D. C. Ralph, R. A. Buhrman, Irrelevance of magnetic proximity effect to the spin-orbit torques in heavy metal/ferromagnet bilayers. *Phys. Rev. B* **98**, 134406 (2018).
23. M.-H. Nguyen, D. C. Ralph, R. A. Buhrman, Spin torque study of the spin Hall conductivity and spin diffusion length in platinum thin films with varying resistivity. *Phys. Rev. Lett.* **116**, 126601 (2016).
24. J. Sinova, S. O. Valenzuela, J. Wunderlich, C. H. Back, T. Jungwirth, Spin Hall effects. *Rev. Mod. Phys.* **87**, 1213–1260 (2015).
25. G. Vignale, Ten years of spin Hall effect. *J. Supercond. Nov. Magn.* **23**, 3–10 (2010).
26. F. Mahfouzi, N. Kioussis, First-principles study of the angular dependence of the spin-orbit torque in Pt/Co and Pd/Co bilayers. *Phys. Rev. B* **97**, 224426 (2018).
27. R. J. Elliott, Theory of the effect of spin-orbit coupling on magnetic resonanceinsomesemiconductors. *Phys. Rev.* **96**, 266–279 (1954).
28. Y. Yafet, *g* factors and spin-lattice relaxation of conduction electrons. *Solid State Phys.* **14**, 1–98 (1963).
29. Y.-T. Chen, S. Takahashi, H. Nakayama, M. Althammer, S. T. B. Goennenwein, E. Saitoh, G. E. W. Bauer, Theory of spin Hall magnetoresistance. *Phys. Rev. B* **87**, 144411 (2013).
30. P. M. Haney, H.-W. Lee, K.-J. Lee, A. Manchon, M. D. Stiles, Current induced torques and interfacial spin-orbit coupling: Semiclassical modeling. *Phys. Rev. B* **87**, 174411 (2013).
31. L. Zhu, D. C. Ralph, R. A. Buhrman, Spin-orbit torques in heavy-metal–ferromagnet bilayers with varying strengths of interfacial spin-orbit coupling. *Phys. Rev. Lett.* **122**, 077201 (2019).
32. C.-F. Pai, Y. Ou, L. H. Vilela-Leão, D. C. Ralph, R. A. Buhrman, Dependence of the efficiency of spin Hall torque on the transparency of Pt/ferromagnetic layer interfaces. *Phys. Rev. B* **92**, 064426 (2015).
33. J.-C. Rojas-Sánchez, N. Reyren, P. Laczkowski, W. Savero, J.-P. Attané, C. Deranlot, M. Jamet, J.-M. George, L. Vila, H. Jaffrès, Spin pumping and inverse spin Hall effect in platinum: The essential role of spin-memory loss at metallic interfaces. *Phys. Rev. Lett.* **112**, 106602 (2014).
34. W. Lin, C. L. Chien, Electrical detection of spin backflow from an antiferromagnetic insulator/$Y_3Fe_5O_{12}$ interface. *Phys. Rev. Lett.* **118**, 067202 (2017).
35. H. An, Y. Kanno, A. Asami, K. Ando, Giant spin-torque generation by heavily oxidized Pt. *Phys. Rev. B* **98**, 014401 (2018).
36. D. A. Svintsitskiy, L. S. Kibis, A. I. Stadnichenko, S. V. Koscheev, V. I. Zaikovskii, A. I. Boronin, Highly oxidized platinum nanoparticles prepared through radio-frequency sputtering: Thermal stability and reaction probability towards CO. *Chem. Phys. Chem.* **16**, 3318–3324 (2015).
37. D. Erts, H. Olin, L. Ryen, E. Olsson, A. Thölén, Maxwell and Sharvin conductance in gold point contacts investigated using TEM-STM. *Phys. Rev. B* **61**, 12725–12727 (2000).
38. Y. Tian, L. Ye, X. Jin, Proper scaling of the anomalous Hall effect. *Phys. Rev. Lett.* **103**, 087206 (2009).
39. L. J. Zhu, D. Pan, J. H. Zhao, Anomalous Hall effect in epitaxial $L1_0$-$Mn_{1.5}$ Ga films with variable chemical ordering. *Phys. Rev. B* **89**, 220406(R) (2014).
40. L. J. Zhu, S. H. Nie, J. H. Zhao, Anomalous Hall effect in $L1_0$–MnAl films with controllable orbital two-channel Kondo effect. *Phys. Rev. B* **93**, 195112 (2016).
41. M. Chen, Z. Shi, W. J. Xu, X. X. Zhang, J. Du, S. M. Zhou, Tuning anomalous Hall conductivity in $L1_0$ FePt films by long range chemical ordering. *Appl. Phys. Lett.* **98**, 082503 (2011).
42. S. Shi, Y. Ou, S. V. Aradhya, D. C. Ralph, R. A. Buhrman, Fast low-current spin-orbit-torque switching of magnetic tunnel junctions through atomic modifications of the free-layer interfaces. *Phys. Rev. Applied* **9**, 011002 (2018).
43. C.-F. Pai, L. Liu, Y. Li, H. W. Tseng, D. C. Ralph, R. A. Buhrman, Spin transfer torque devices utilizing the giant spin Hall effect of tungsten. *Appl. Phys. Lett.* **101**, 122404 (2012).
44. L. Liu, C.-F. Pai, Y. Li, H. W. Tseng, D. C. Ralph, R. A. Buhrman, Spin-torque switching with the giant spin Hall effect of tantalum. *Science* **336**, 555–558 (2012).
45. W. Jiang, P. Upadhyaya, W. Zhang, G. Yu, M. B. Jungfleisch, F. Y. Fradin, J. E. Pearson, Y. Tserkovnyak, K. L. Wang, O. Heinonen, S. G. E. te Velthuis, A. Hoffmann, Blowing magnetic skyrmion bubbles. *Science* **349**, 283–286 (2015).
46. A. R. Mellnik, J. S. Lee, A. Richardella, J. L. Grab, P. J. Mintun, M. H. Fischer, A. Vaezi, A. Manchon, E.-A. Kim, N. Samarth, D. C. Ralph, Spin-transfer torque generated by a topological insulator. *Nature* **511**, 449–451 (2014).
47. M. DC, R. Grassi, J.-Y. Chen, M. Jamali, D. R. Hickey, D. Zhang, Z. Zhao, H. Li, P. Quarterman, Y. Lv, M. Li, A. Manchon, K. Andre Mkhoyan, T. Low, J.-P. Wang, Room-temperature high spin–orbit torque due to quantum confinement in sputtered $Bi_xSe_{(1-x)}$ films. *Nat. Mater.* **17**, 800–807 (2018).
48. D. S. Holmes, A. L. Ripple, M. A. Manheimer, Energy-efficient superconducting computing—Power budgets and requirements. *IEEE Trans. Appl. Supercond.* **23**, 1701610 (2013).
49. O. J. Lee, L. Q. Liu, C. F. Pai, Y. Li, H. W. Tseng, P. G. Gowtham, J. P. Park, D. C. Ralph, R. A. Buhrman, Central role of domain wall depinning for perpendicular magnetization switching driven by spin torque from the spin Hall effect. *Phys. Rev. B* **89**, 024418 (2014).
50. S. Fukami, T. Anekawa, C. Zhang, H. Ohno, A spin–orbit torque switching scheme with collinear magnetic easy axis and current configuration. *Nat. Nanotechnol.* **11**, 621–625 (2016).

Acknowledgments

Funding: This work was supported, in part, by the Office of Naval Research (N00014-15-1-2449), by the NSF MRSEC program (DMR-1719875) through the Cornell Center for Materials Research and by the Office of the Director of National Intelligence (ODNI), Intelligence Advanced Research Projects Activity (IARPA), via contract W911NF-14-C0089. The views and conclusions contained herein are those of the authors and should not be interpreted as necessarily representing the official policies or endorsements, either expressed or implied, of the ODNI, IARPA, or the U.S. Government. The U.S. Government is authorized to reproduce and distribute reprints for Governmental purposes notwithstanding any copyright annotation thereon. The devices were fabricated, in part, at the Cornell NanoScale Facility, an NNCI member supported by NSF Grant No. ECCS-1542081. The TEM measurements performed at Shaanxi Normal University and Beijing University of Technology were supported by the Science and Technology Program of Shaanxi Province (Grant No. 2019JQ-433) and the Fundamental Research Funds for the Central Universities (Grant No. GK201903024). **Author contributions:** Lijun Zhu and R.A.B designed the project. Lijun Zhu, R.A.B., and D.C.R. wrote the manuscript draft. Lijun Zhu fabricated the samples and performed the sample fabrication, vibrating sample magnetometry, XRD, XPS, and spin-torque measurements. Lujun Zhu and M.S. performed the TEM measurements. All the authors contributed to discussing the results and writing the manuscript. **Competing interests:** The authors declare that they have no competing interests. **Data and materials availability:** All data needed to evaluate the conclusions in the paper are present in the paper and/or the Supplementary Materials. Additional data related to this paper may be requested from the authors.

Submitted 21 October 2018
Accepted 14 June 2019
Published 19 July 2019
10.1126/sciadv.aav8025

Citation: L. Zhu, L. Zhu, M. Sui, D. C. Ralph, R. A. Buhrman, Variation of the giant intrinsic spin Hall conductivity of Pt with carrier lifetime. *Sci. Adv.* **5**, eaav8025 (2019).

Variation of the giant intrinsic spin Hall conductivity of Pt with carrier lifetime

Lijun Zhu, Lujun Zhu, Manling Sui, Daniel C. Ralph and Robert A. Buhrman

Sci Adv **5** (7), eaav8025.
DOI: 10.1126/sciadv.aav8025